Induced Power of the Helicopter Rotor

Robert A. Ormiston

Army/NASA Rotorcraft Division
Aeroflightdynamics Directorate (AMRDEC)
US Army Research, Development, & Engineering Command
Ames Research Center, Moffett Field, California

Abstract

A simplified rotor model was used to explore fundamental behavior of lifting rotor induced power at moderate and high advance ratios. Several rotor inflow theories, including dynamic inflow theory and prescribed-wake vortex theory, together with idealized notional airfoil stall models were employed. A number of unusual results were encountered at high advance ratios including trim control reversal and multiple trim solutions. Significant increases in rotor induced power (torque) above the ideal minimum were observed for moderately high advance ratio. Very high induced power was observed near and above unity advance ratio. The results were sensitive to the stall characteristics of the airfoil models used. An equivalent wing analysis was developed to determine induced power from Prandtl lifting line theory and help interpret the rotor induced power behavior in terms of the spanwise airload distribution. The equivalent wing approach was successful in capturing the principal variations of induced power for different configurations and operating conditions. The effects blade root cutout were found to have a significant effect on rotor trim and induced power at high advance ratios.

Introduction

The conceptual simplicity of the helicopter belies the complexity of the flowfield of the lifting rotor. Although separation, reverse flow, compressibility, and blade vortex interaction are important phenomena, the flowfield induced by the lifting rotor blades is especially complex and it is arguably the dominant feature of rotor aerodynamics. The induced flowfield determines, in large measure, the performance, dynamic loads, and flight control characteristics of the helicopter.

There are a number of interesting aspects of the rotor inflow and induced power that are relevant to rotorcraft engineering. An essential problem in rotor aerodynamics is determining the power required to generate thrust and the induced power is the principal contributor in hover and low-to-moderate flight speeds. The ideal minimum power decreases inversely with flight speed and is commonly considered to be relatively unimportant in high-speed forward flight. However, due to non-uniform distribution of airload and inflow, the non-ideal induced power may be considerable at higher flight speeds, Ref. 1. This may be an important consideration in performance analysis in moderate- and high-speed flight, especially for future advanced rotorcraft emphasizing increased speed and efficiency, Ref. 2.

Fundamental understanding of rotor induced inflow and induced power contributes to practical engineering knowledge needed to develop advanced rotors with minimum induced power. Analytical methods for predicting rotor inflow and induced power based on fundamental theory provide the basic ingredient for design methodology. Fundamental understanding of lifting rotor induced power and the influence of the airload and inflow distributions is relatively limited, mainly due to the complexity of the problem. This stands in marked contrast to conventional fixed wing aerodyamics. For example, current theory offers few insights into the question of the minimum induced power of a rotor, beyond the elementary concepts of uniform inflow momentum theory. Basic rotor parameters, including blade number, twist, solidity, planform, as well as trim, blade mechanics, hub moments, higher harmonic blade pitch, etc. are not easily characterized in terms of their effect on induced power. Active control, HHC/IBC, and variable geometry design concepts may be difficult to exploit for improving rotor performance unless they can be understood in terms of reducing the non-ideal induced power. Previous work on the problem of minimizing rotor induced power includes classical Goldstein rotor theory for the optimum loading of a lightly loaded rotor in axial flow. More recently, Moffitt and Bissell, Ref.

3; Quackenbush et al, Ref. 4; Hall et al, Ref. 5; and Rand et al, Ref. 6 addressed the problem of minimizing rotor induced power.

In contrast to rotor theory, conventional fixed-wing theory provides considerable insight about the basic effects of the spanwise airload distribution on induced drag. Prandtl's classical lifting line theory succinctly and elegantly captures the essential features of fixed-wing aerodynamics, illuminating the principal phenomena, as well as providing a practical engineering analysis tool. An analogous theory is not available for the lifting rotor.

Any quantitative investigation of rotor induced power must consider the wake induced inflow theory or computational model, of which numerous approaches are available. These range from sophisticated CFD numerical methods and various discrete vortex filament methods with prescribed and free-wake geometry with periodic and time accurate methods, Ref. 7, to potential flow methods such as finite state dynamic inflow theory, Ref. 8, and ending with simple momentum theories. For analytical methods, accuracy and computational efficiency are the important considerations. CFD and vortex wake methods are the most accurate, but are computationally intensive, while momentum theory offers no capability to predict the non-ideal portion of rotor induced power. Finite state dynamic inflow theory offers an analytical formulation and the opportunity to predict induced power but there has been little exploration of accuracy versus computational efficiency tradeoffs.

The paper will focus on the fundamentals of rotor induced power and induced inflow modeling in forward flight. The objective is to increase understanding of rotor induced power and its relation to the airload distribution. Fixed wing lifting line theory will be adapted to analyze rotor induced power and to explore parallels between the rotor and fixed wing induced power. Another objective will be to explore and compare the capabilities of different rotor inflow models for the induced power problem. Dynamic inflow theory combines a unique balance of physical accuracy and analytical utility that offers an opportunity to advance our fundamental understanding of rotor induced power. The conventional numerical prescribed-wake vortex method will be used to compare results from dynamic inflow. The fundamental objectives will include exploring the behavior of the induced power of a lifting rotor to determine the magnitude of non-ideal induced power at moderate and high advance ratio. Specific questions involve the behavior near $\mu = 1.0$: Is there a peak power and how does the power vary beyond $\mu = 1.0$?

The paper is organized to address the analysis approach; basic trim and induced power based on the momentum theory uniform inflow model; dynamic inflow theory induced power results; vortex wake induced power results and comparisons with dynamic inflow; development of an equivalent wing approach based on Prandtl lifting line theory; presentation of spanwise airloads and induced power results for the equivalent wing calculations; and conclusions. Throughout the paper, the terms induced power and induced torque are uses somewhat interchangeably, depending on the context.

Analysis Approach

The analysis deals with the forces and moments (induced torque) of an idealized rotor system, simplified to the bare essentials needed for the present purposes. All results were calculated with the U.S. Army's Rotorcraft Comprehensive Analysis System, Ref. 9. RCAS provides a wide variety of structural and aerodynamics modeling capabilities well suited for the present purposes. Several different aerodynamic inflow models are available for comparisons in regard to rotor induced power. The discrete vortex filament prescribed wake model option used for the present results is the University of Maryland time accurate method reported in Ref. 7. For present purposes, the prescribed wake was preferred over the alternative free wake. The Peters-He finite state dynamic inflow theory, Ref. 8, was used including several models of varying fidelity. Uniform inflow was used as a comparison baseline. All other aerodynamic analysis details were treated in the most elementary manner possible: simple incompressible linear 2-D thin airfoil theory was used for an airfoil without profile drag or unsteady aerodynamic effects. The purpose of this approach was to eliminate all unnecessary factors from the phenomena of interest in order to focus on fundamental behavior and simplify the interpretation of the results as much as possible.

The rotor configuration comprised four straight, untwisted, rigid blades, without hinges at the blade root. Thus no blade unsteady motion was present, except for rotor blade rotation and the trim collective and cyclic pitch control angles. Two blade root cutout values were included, zero and 20%R. For the blade without root cutout, the solidity was 0.10. The blade was discretized into 31 radial aerosegments with finer concentration of aerosegments at the tip and the root of the blade.

The rotor shaft angle of attack was zero for all forward flight velocities and the trim condition was 5,000-lb thrust with zero pitch and roll hub moments. The rotor

reaction forces therefore include thrust (lift), drag, side force, and pitch, roll, and yaw (shaft torque) moments. The induced power is reflected in the shaft torque and the longitudinal rotor force. The principal rotor analysis results are presented for a range of flight speeds from zero to 800 ft/sec. For the rotor tip speed of 600 ft/sec, the highest advance ratio is 1.33.

In keeping with reducing the rotor model properties to the simplest needed to address basic phenomena in the clearest way possible, three different idealized airfoil models were used to define the 2-D lift coefficient variation with angle of attack. These include basic linear airfoil theory as well as two arbitrary airfoil stall models. The airfoil maximum lift coefficient has a significant influence on the behavior of a rotor producing thrust at high advance ratio. The three models are denoted as AF1, AF2, and AF3.

For the linear airfoil model, AF1, lift is proportional to angle of attack and the airfoil is assumed not to stall at any angle of attack. This may be possible to represent for analyses where the angle of attack remains small, however, a rotor blade airfoil operates throughout the full 360 degree range of angle of attack in the reverse flow region. In order for the lift curve slope to be constant at all angles of attack, the lift coefficient must be discontinuous at some point. This makes most sense at $|\alpha| = \pi/2$ and leads to a maximum value of π^2. The variation of lift coefficient with angle of attack for the AF1 model may be expressed as:

$$
\begin{aligned}
C_l &= 2\pi(\alpha + \pi) & -\pi \leq \alpha \leq -\tfrac{\pi}{2} \\
C_l &= 2\pi\alpha & -\tfrac{\pi}{2} \leq \alpha \leq \tfrac{\pi}{2} \\
C_l &= 2\pi(\alpha - \pi) & \tfrac{\pi}{2} < \alpha \leq \pi \\
C_{l\max_1} &= \pi^2 \quad at \quad \alpha = \tfrac{\pi}{2}
\end{aligned} \tag{1}
$$

The second airfoil model, denoted AF2, was defined to limit the maximum lift at $\alpha = \pi/4$ and to be continuous at $|\alpha| = \pi/2$. It may be expressed as:

$$
\begin{aligned}
C_l &= \pi \sin 2\alpha \\
C_{l\max_2} &= \pi \quad at \quad \alpha = \tfrac{\pi}{4}
\end{aligned} \tag{2}
$$

The third airfoil model, denoted AF3, provides more realistic stall behavior than the AF2 model and is expressed by a series of piecewise linear segments:

$$
\begin{aligned}
C_l &= 2\pi(\alpha + \pi) & -\pi \leq \alpha \leq -\tfrac{11\pi}{12} \\
C_l &= -\tfrac{6}{5\pi}C_{l_m}(2\alpha + \pi) & -\tfrac{11\pi}{12} < \alpha < -\tfrac{\pi}{12} \\
C_l &= 2\pi\alpha & -\tfrac{\pi}{12} \leq \alpha \leq \tfrac{\pi}{12} \\
C_l &= -\tfrac{6}{5\pi}C_{l_m}(2\alpha - \pi) & \tfrac{\pi}{12} < \alpha < \tfrac{11\pi}{12} \\
C_l &= 2\pi(\alpha - \pi) & \tfrac{11\pi}{12} \leq \alpha \leq \pi
\end{aligned} \tag{3}
$$

$$
C_{l\max_3} = \frac{\pi^2}{6} = 1.6449 \quad at \quad \alpha = \tfrac{\pi}{12}
$$

The lift coefficient variation with angle of attack for the three airfoil models are shown together in Fig. 1 to highlight the different characteristics. Although the linear airfoil model, AF1, was intended to avoid the complications of airfoil stall behavior for the most elementary rotor analysis cases, the presence of a maximum lift coefficient, even a large value, will be evident in trim and rotor power results at some value of rotor lift, or at some values of advance ratio. The second airfoil model, AF2, represents a convenient analytical representation having continuous variations with angle of attack and no discontinuities in lift curve slope although the maximum lift coefficient is unrealistically high compared to real airfoils. The third airfoil model, AF3, was included for cases where the effects of stall were of primary interest and it characterizes basic stall behavior with a simple model.
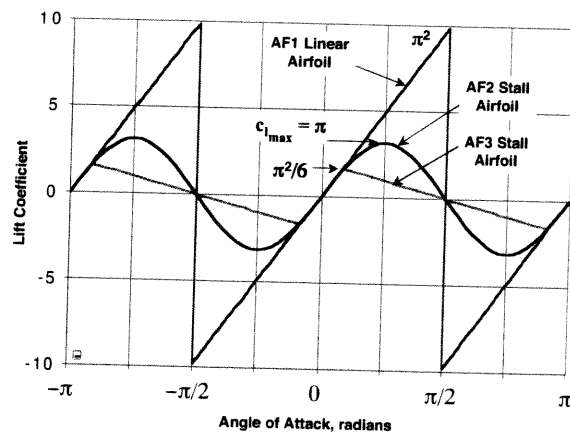

Fig. 1. 2-D airfoil lift coefficient versus 360 degree angle of attack range for three idealized airfoil models, linear airfoil AF1 and stall airfoil models AF2 and AF3.

Basic Trim and Power Characteristics - Uniform Inflow

To generate a specified level of thrust with zero pitch and roll moment trim requires that the rotor collective and cyclic pitch vary with forward velocity. At high advance ratio, these trim control values will become large and sensitive to many blade configuration and

modeling variables. Before introducing the principal results, the rotor trim control characteristics will be presented, including the associated induced power characteristics. For simplicity, elementary momentum theory uniform inflow will be used. The discussion will focus on the effects of blade airfoil stall modeling and blade root cutout, both of which are major factors for trim at high advance ratio. For the rotor with blade root cutout, Figs. 2 and 3 show the variation of collective pitch and lateral cyclic pitch ($\sin(\psi)$) with advance ratio for the three different airfoil stall models. Corresponding trim results to examine the effects of blade root cutout will presented in Figs. 4 and 5.
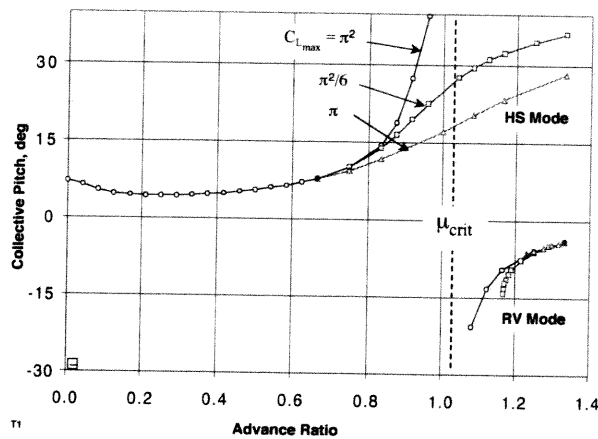

Fig. 2. Trim collective pitch versus advance ratio for three airfoil models, with blade root cutout and uniform inflow.
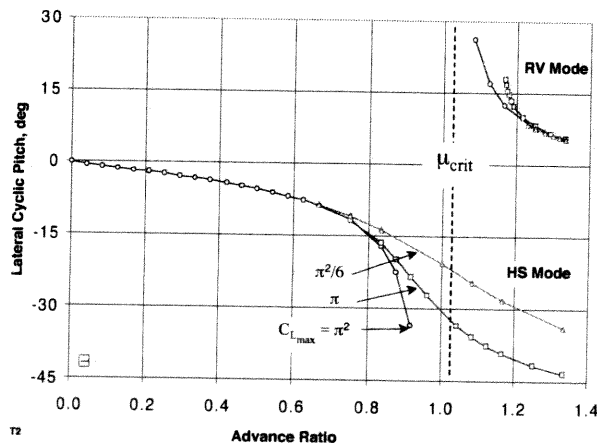

Fig. 3. Trim lateral cyclic pitch versus advance ratio for three airfoil models, with blade root cutout and uniform inflow.
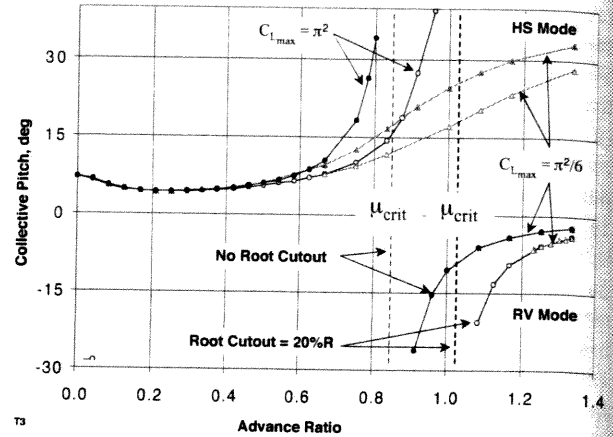

Fig. 4. Effect of blade root cutout on trim collective pitch with linear and stall airfoil models, AF1 and AF3, and uniform inflow.
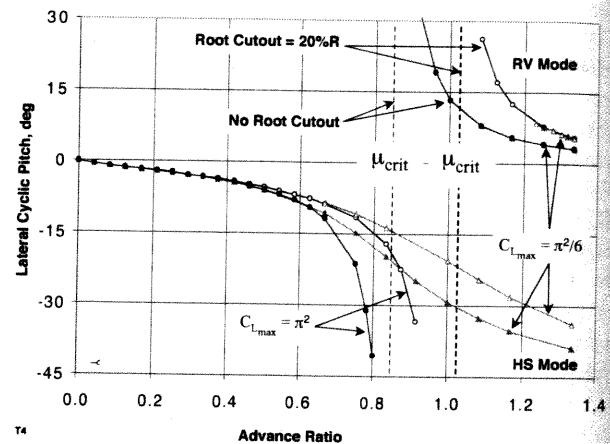

Fig. 5. Effect of blade root cutout on trim lateral cyclic pitch with linear and stall airfoil models, AF1 and AF3, and uniform inflow.

To maintain 5000 lb constant thrust, the collective pitch first decreases from hover but then increases with advance ratio in the familiar fashion due to reduced velocity on the retreating blade and negative lift in the reverse flow region, Fig. 2. Lateral cyclic pitch increases with advance ratio to maintain roll moment trim, Fig. 3, (longitudinal cyclic pitch, $\cos(\psi)$, is zero for uniform inflow). Both collective and cyclic pitch begin to increase rapidly as advance ratio approaches 1.0 and the retreating blade lift capability is diminished by the rapidly enlarging reverse flow region. The advancing blade lift is correspondingly reduced by lateral cyclic pitch required to maintain roll moment equilibrium. As advance ratio approaches 1.0, the trim control behavior becomes very sensitive to the blade airfoil model stall characteristics. For the simple "linear" airfoil model, AF1, the trim collective and cyclic pitch increase steeply until reaching a "critical

36

advance ratio" (μ_{crit}) near 1.0 and then reverse sign in a discontinuous fashion. In effect, the rotor switches to an alternate mode of operation where negative collective pitch and positive lateral cyclic pitch produce positive advancing blade pitch and negative retreating blade pitch. The retreating blade generates positive lift in the reverse flow region since the airfoil "flies trailing-edge-up" into the relative wind. This mode of operation shares some similarity with the so-called "reverse velocity rotor" high speed rotorcraft concept, Ref. 10, and for present purposes will be referred to as the RV mode.

The rotor trim results for the alternative airfoil stall models show markedly different behavior, including non-unique, multiple trim states. The collective and cyclic pitch variations at high advance ratio for the two stall airfoil models AF2 and AF3 do not exhibit the discontinuous control reversal behavior of the linear

airfoil AF1, and, in fact, exhibit smooth, continuously increasing trim values with advance ratio. The different trim values of the two stall airfoils reflect the different $C_{l\max}$ values of AF2 and AF3, in particular. In addition to this "high speed" (HS) trim mode, the AF2 and AF3 stall airfoils also exhibit trim in the RV mode, with reversed control trim values very similar to the linear airfoil model, AF1. In fact this is to be expected as all three airfoils have identical lift coefficients at small angles of attack.

The effects of blade root cutout, are shown in Figs. 4 and 5, do not alter the basic airfoil-model-dependent trim behavior described above. However, the value of critical advance ratio, where the linear airfoil result switches from the HS mode to the RV mode, is increased by blade root cutout.
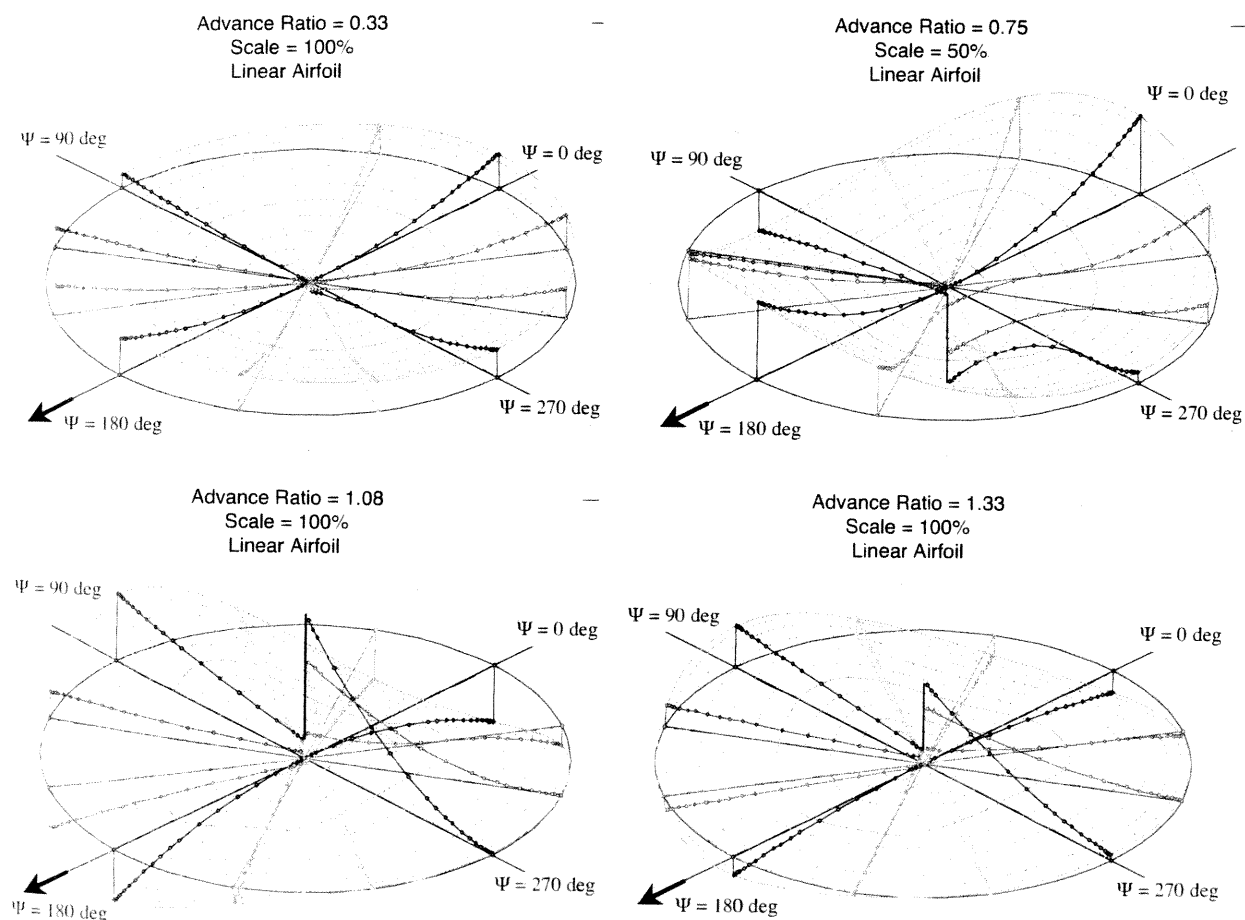
Advance Ratio = 0.33
Scale = 100%
Linear Airfoil

Advance Ratio = 0.75
Scale = 50%
Linear Airfoil

Advance Ratio = 1.08
Scale = 100%
Linear Airfoil

Advance Ratio = 1.33
Scale = 100%
Linear Airfoil

Fig. 6 - 9. **Progression of rotor disk airload distribution with advance ratio for the linear airfoil model, uniform inflow, no blade root cutout.**

The two different modes of operation at high advance ratio may be described as follows. At low advance ratios (and independent of the airfoil stall model) the rotor compensates for the loss of lift capability in the reverse flow region by increasing the loading of the rotor at the front and rear of the disk. At higher advance ratios, the effect of the airfoil stall model becomes important. With the stall airfoil models, AF2 & AF3, the fore-aft load re-distribution progresses continuously with advance ratio, while the advancing and retreating blades begin to carry increasing large negative lift. At the highest advance ratios, the rotor thrust reflects the difference between large opposing airloads acting on different regions of the rotor disk. With the linear airfoil model, AF1, the increased fore and aft loading reaches a limit at the critical advance ratio, beyond which the rotor switches to the RV mode and the lift is carried on the advancing and retreating sides of the disk while the fore and aft regions of the rotor become negatively loaded.

This behavior is illustrated by the distribution of the rotor airloads on the rotor disk for the linear airfoil model and for the stall airfoil model AF3 in Figs. 6-9 and Figs. 10-13, respectively. The examples are for the blade without root cutout and show the progression of the loading as the advance ratio is increased. The relative scale is adjusted to accommodate the rapid airload variations near the critical advance ratio. At the lowest advance ratio the loading distributions for both airfoil models are identical. At 0.75 advance ratio, large differences in the negative loading of the inboard retreating blade are apparent as the front and rear portions of the disk load up. The fore and aft loading trend continues progressively for the stall airfoil model while the linear airfoil model reverses the loading from the fore and aft to side-to-side of he RV mode. At high advance ratios, the stall airfoil model load distribution in the HS mode shows the fore-aft loading shifted toward the advancing blade side of the rotor to offset the roll moment of the large negative loading of the advancing blade. Not shown is the RV mode trim solution for the stall airfoil rotor since the airload distributions are nearly identical to the linear airfoil model rotor.

Advance Ratio = 0.33
Scale = 100%
Stall Airfoil

$\Psi = 90$ deg $\Psi = 0$ deg

$\Psi = 180$ deg $\Psi = 270$ deg

Advance Ratio = 0.75
Scale = 50%
Stall Airfoil

$\Psi = 90$ deg $\Psi = 0$ deg

$\Psi = 180$ deg $\Psi = 270$ deg

Advance Ratio = 1.08
Scale = 40%
Stall Airfoil

$\Psi = 90$ deg $\Psi = 0$ deg

$\Psi = 180$ deg $\Psi = 270$ deg

Advance Ratio = 1.33
Scale = 40%
Stall Airfoil

$\Psi = 90$ deg $\Psi = 0$ deg
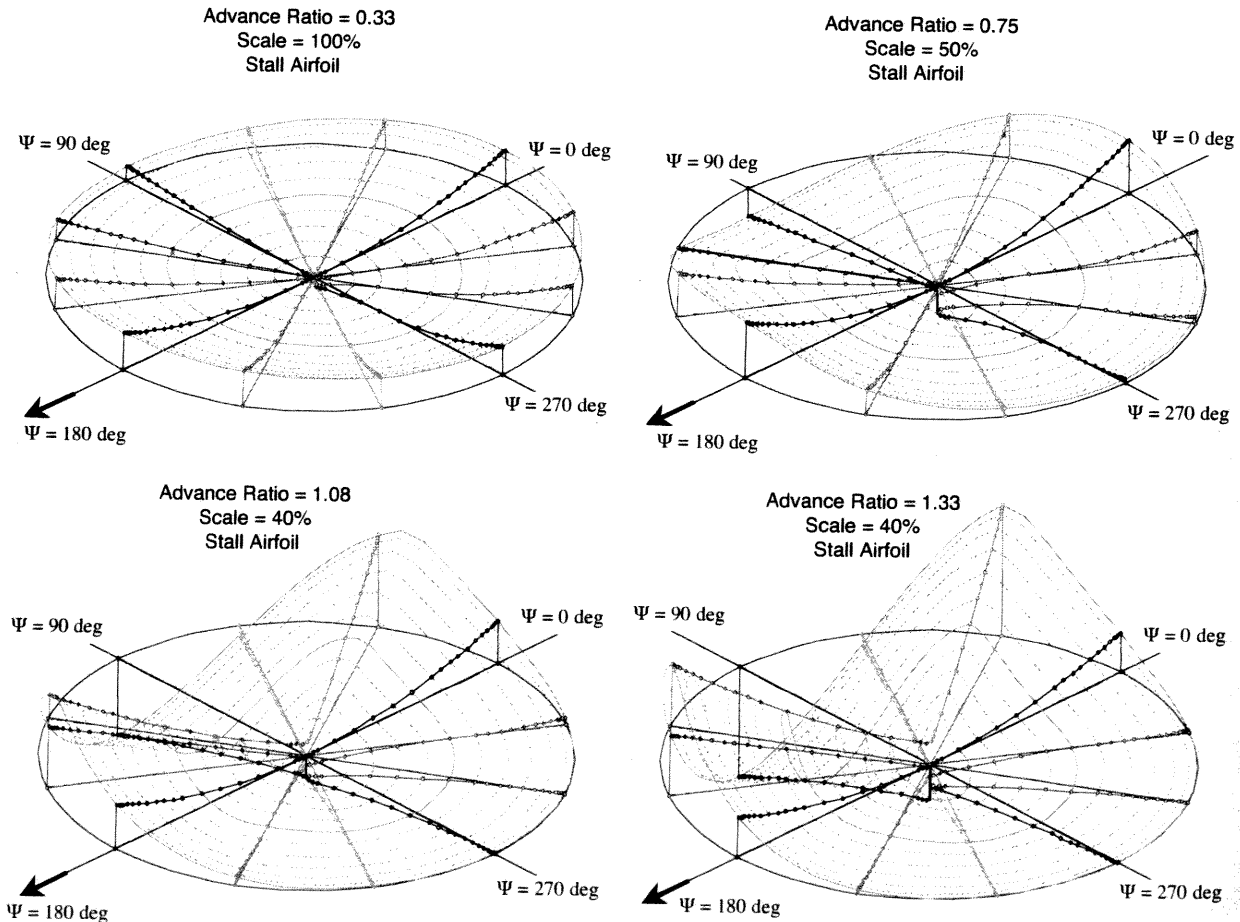
$\Psi = 180$ deg $\Psi = 270$ deg

Fig. 10 - 13. Progression of rotor disk airload distribution with advance ratio for the AF3 airfoil stall model, uniform inflow, no blade root cutout.

The explanation for the different HS and RV mode trim characteristics at high advance ratios is not so simple but likely depends on the interplay of the 1/rev blade pitch-constrained radial and azimuthal airloads (local peaks dependent on stall model) and the rotor trim constraints (thrust, pitch, and roll moment). Variations in the maximum lift coefficient of different airfoil models probably determine which combinations of pitch control angles will satisfy the trim constraints and thus drive the trim solution. Clearly, higher harmonic variations of blade pitch could redistribute the airloads and produce other trim modes.

It should be noted that relatively idealized airfoil models were chosen for the present investigation to focus on fundamentals and to facilitate interpretation of the results. Since the trim characteristics are sensitive to these airfoil properties, and actual airfoils differ in important respects from the idealized models, the present results may differ from actual rotor behavior in important respects.

Rotor Torque, Drag, and Effective Torque

The present results were obtained for an idealized rotor with rigid blades operating at zero shaft angle of attack in order to simplify interpretation of local blade velocity and airload components. Trimming the rotor to a specified thrust and zero hub moments yielded resultant shaft torque and rotor longitudinal and lateral forces. While these three quantities are individually of interest, the induced power required by the rotor to produce a specified thrust (without a propulsive or drag force) is of principal interest in this paper. This may be determined from the shaft torque, Q, and rotor longitudinal force, F_x. The resulting total rotor power, expressed as the effective torque, Q_e, is given by:

$$Q_e = Q + F_x V / \Omega \qquad (4)$$

To briefly illustrate how these quantities reflect the trim characteristics and vary with blade stall model, a few results are presented using elementary momentum theory uniform inflow for the rotor configuration with no blade root cutout. Figure 14 shows the rotor longitudinal force as a function of advance ratio, where a positive value represents a drag force. Interestingly, for the rigid rotor at zero shaft angle, the longitudinal force at low advance ratio is a propulsive force. This is caused by the lower induced drag component of the airfoil lift on the advancing blade (directed rearward) compared to the retreating blade at the same radius (higher drag, acting forward). This is easily understood in the case of uniform inflow where the induced flow angle for the advancing blade will be lower due to the

higher local flow velocity than the retreating blade with a lower relative local flow velocity. Near the critical advance ratio, the propulsive force increases and then decreases again for the two stall airfoil models. For the linear airfoil model, the longitudinal force reverses and becomes a drag force as the rotor switches from the HS mode to the RV mode. Here, the larger retreating blade drag acts in the rearward direction and adds to the advancing blade drag.
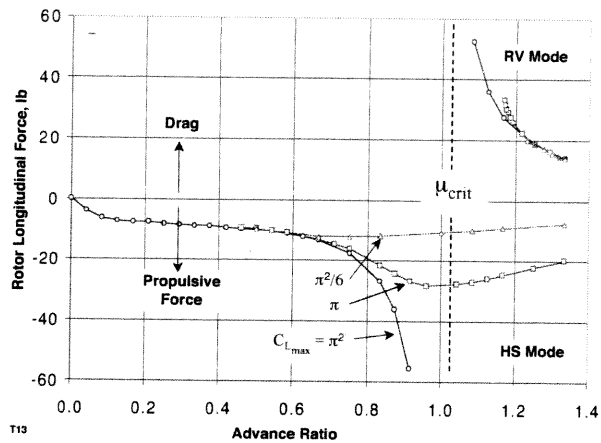

Fig. 14. Rotor longitudinal force versus advance ratio for three airfoil models, with blade root cutout and uniform inflow.

The rotor shaft torque in Fig. 15 shows the expected decrease with velocity at low advance ratio, but increases near the critical advance ratio. The linear airfoil model, again, shows a reversal in shaft torque at the critical advance ratio. The similarity between the rotor force and torque trends with advance ratio and the corresponding collective and lateral cyclic trim control trends in Figs. 2-3 may be noted.
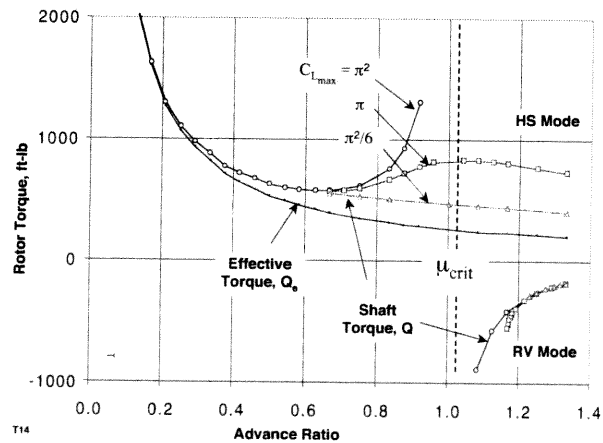

Fig. 15. Rotor shaft torque and effective torque versus advance ratio from uniform inflow for three airfoil models, with blade root cutout.

39

Figure 15 also includes the effective rotor torque obtained from Eq. (4). In fact, the result reduces to the ideal induced rotor torque (minimum power) associated with momentum theory uniform inflow, for all airfoil stall models, as it should. The ideal induced power decreases continuously with velocity and except for hover and very low advance ratio, and is be given by

$$Q_e = T^2 /(2\pi\rho\Omega^2 R^3 \mu) \tag{5}$$

Results to be presented in the following sections are based on nonuniform inflow analyses reflect the influence of the nonuniform distribution of induced velocity and therefore will depart from this ideal minimum effective torque obtained with uniform inflow.

Dynamic Inflow Analysis and Results

Dynamic inflow is the commonly used name for a rotor wake inflow theory evolved over many years by Professor D. A. Peters and his students. The first and simplest dynamic inflow theories are based on momentum theory, Refs. 11-13, but the earliest theory for steady nonuniform inflow for a rotor was initiated by Mangler, Ref. 14, based on potential flow theory for a circular wing by Kinner, Ref. 15. A significant extension of this work, including the unsteady inflow for the first harmonic loading functions, was developed by Pitt & Peters, Ref. 16 and formed the basis for what has come to be generally known as dynamic inflow. Dynamic inflow theory is based on solutions of linear, incompressible, potential flow for the unsteady flowfield induced by an arbitrarily loaded circular disk in either axial or oblique flow. The pressure loading on the disk is represented by a series of radial and azimuthal loading functions and the theory provides the corresponding radial and azimuthal induced velocity functions associated with each pressure loading function. Extensions of the Pitt and Peters theory to an arbitrary number of radial and azimuthal loading functions, leading to Generalized Dynamic Wake Theory was accomplished by Peters and He, Ref. 8. A variety of other refinements and applications have been accomplished. The correspondence between the most complete dynamic inflow theory and other classical potential flow solutions for 2-D thin airfoil theory (Glauert and Theodorsen), 3-D finite wing lifting line theory (Prandtl), and rotor theories (Goldstein, Prandtl, and Loewy), has been established in Refs. 17 - 19.

A unique feature of dynamic inflow theory is that the equations for the rotor loading and inflow distribution functions are expressed as finite states in ordinary differential equations making them particularly compatible with standard formulations of aeroelastic, flight control, and control system analyses for rotorcraft. It provides a rigorous, relatively high fidelity, representation of rotor airloads and induced flow characteristics and has found wide application for these disciplines. Dynamic inflow theory has been less commonly applied for analysis of rotor blade airloads and structural loads because of the prevalence of nonlinear aerodynamic phenomena for many operating conditions, but the theory provides considerable value where reasonable accuracy and reduced computation time is important. Although the rigorous theoretical foundation and the fidelity of the rotor wake inflow should be advantageous for rotorcraft performance analysis, this potential has not been extensively exploited. This provides one of the underlying motivations for the present investigation. In addition, the analytical formulation of dynamic inflow theory in terms of airload and induced inflow functions offers the possibility that analytical solutions for the induced power of a helicopter may be developed.

Induced Torque Results Based on Dynamic Inflow

The theory of dynamic inflow was described in an earlier section as well as some of the potential benefits of the theory for calculating rotor induced power, one of these being the ability to tailor the inflow modeling fidelity to the needs of the problem at hand.
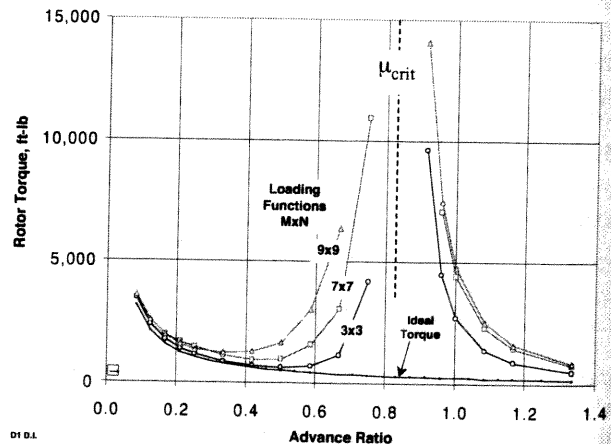

Fig. 16. Variation of rotor effective torque versus advance ratio with number of dynamic inflow loading functions, the linear airfoil modelAF1 and no blade root cutout.

The first results, Fig. 16, will illustrate the basic effect of advance ratio on the effective torque and, in addition, how the effective rotor torque is influenced by the number of radial and azimuthal loading functions included in the calculations. The blade without root cutout is used with the linear airfoil model and three combinations of dynamic inflow loading functions, MxN =3x3, 7x7, and 9x9. The results differ markedly

40

from the effective torque results presented earlier for uniform inflow. Now the effects of nonuniform inflow, varying with advance ratio, produce an increment of induced torque over and above the ideal minimum based on momentum theory uniform inflow. The basic reduction in induced torque with advance ratio at low speeds is offset by the increase in non-ideal induced power to the extent that, between $\mu = 0.25$ and 0.5, the total induced torque begins to increase with advance ratio. This may be attributed to the increasingly nonuniform distribution of airload over the rotor disk associated with the effects of the reverse flow region and the azimuthal blade pitch variations due to the collective and cyclic pitch needed to trim the rotor. Equally important are the variations in induced velocity accompanying the nonuniform airload distribution.

As the advance ratio increases toward 1.0, the increased induced torque becomes very large and appears to diverge at an advance ratio lower than 1.0 that was termed the critical advance ratio in the earlier discussion of the trim characteristics of the rotor using uniform inflow. This "divergence" in rotor induced torque coincides with the reversal in collective and longitudinal pitch required for trim. For advance ratios beyond the critical value, the induced torque rapidly decreases and begins to approach the ideal trend for advance ratios well beyond 1.0. It may be noted that the induced torque remains at a level several times higher than the ideal minimum at advance ratio 1.33 (for the 9x9 dynamic inflow model).

These results raise several interesting issues. The induced torque at the critical advance ratio remains undetermined and it is of theoretical interest to know the value of this peak torque. And whether the peak torque occurs at the critical advance ratio. Or even whether the variation of torque is continuous in the region of the critical advance ratio. In practice, the induced torque is difficult to determine in the vicinity of the critical advance ratio because of the difficulty in finding numerical solutions for the trim controls. Finally, it is clear that these issues are associated with the impact of the reverse flow region at these operating conditions and the effect on the lift producing capability of the rotor near the critical advance ratio. Clearly, the maximum lift capability of the rotor must decrease and perhaps even vanish at the critical advance ratio and it must be kept in mind that the present results are obtained for a rotor that is constrained to maintain a constant level of thrust. Important related factors are the blade airfoil stall characteristics and size of the rotor blade root cutout that will be explored in more detail below.

The induced torque results in Fig. 16 show considerable variation depending on the number of dynamic inflow

loading functions included in the solution. In fact the solution converges with increasing values of MxN but the convergence is relatively slow. The convergence is more rapid for the lowest and highest advance ratios where the reverse flow region nonuniformities are least pronounced and the additional loading functions needed to represent these nonuniformities become less important. While additional investigation is warranted on the issue of convergence, the 9x9 dynamic inflow model is considered most appropriate for the present purposes and this model will be used for subsequent parameter investigations and comparisons with other induced inflow models. As a final comment, it is noted that the induced power increases with the number of loading functions. This is qualitatively consistent with the notion that non-ideal induced power is a consequence of the degree of nonuniformity of the airload distribution. Therefore, the 3x3 dynamic inflow model, which is capable of representing only the lower order loading nonuniformities, shows only a small increase in induced torque at low and moderate advance ratios.
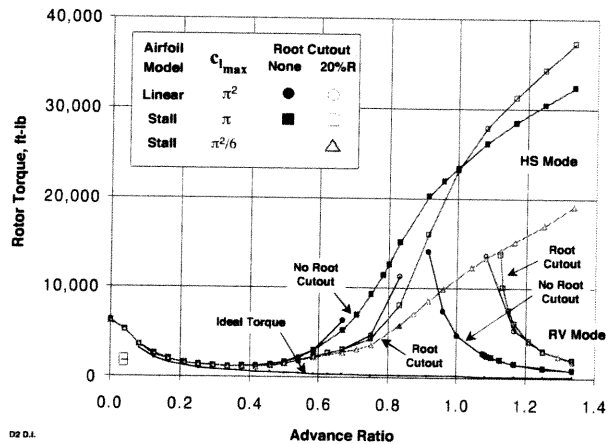

Fig. 17. Rotor effective torque versus advance ratio from 9x9 dynamic inflow model; effect of blade root cutout and three airfoil models.

The 9x9 dynamic inflow model is used to address the effects of blade root cutout and airfoil stall model on induced power and the results are presented in Fig. 17. The effects of blade root cutout may be seen by comparing the linear airfoil model results in Figs. 17 and 16 with and without root cutout. The principal effect is that root cutout increases the critical advance ratio. The practical impact of root cutout is that it significantly reduces the induced torque for high advance ratios below the critical advance ratio but that it significantly increases induced power at advance ratios above μ_c. Thus, a conventional helicopter optimized for high speed may benefit substantially from blade root cutout.

Figure 17 augments the linear airfoil results of Fig. 16 with the two airfoil stall models, AF2 and AF3. As in the case of uniform inflow, the airfoil stall models fundamentally alter the trim behavior of the rotor using dynamic inflow and the trends (not show here) are similar to the uniform inflow results. However, unlike uniform inflow, the effects of the airfoil stall models on effective torque for the dynamic inflow models are significant. Specifically, the induced torque with both airfoil stall models shows two solutions at high advance ratio, one branch (the HS mode) that merges with the linear airfoil model results at low advance ratio but increases continuously - without diverging at the critical advance ratio - to a high induced torque value at the highest advance ratio. The second induced torque solution branch exhibits much lower torque levels (the RV mode) and merges with the high advance ratio solution for the linear airfoil model as advance ratio increases. One difference, however, is that the minimum advance ratio for the RV mode of the stall airfoil models is higher than the minimum advance ratio of the linear stall model.

The reason for the high induced torque of the HS mode branch for the stall airfoil models at high advance ratio in Fig. 17 is due to the fact that the loading is increasingly concentrated at the front and rear of the rotor disk while the advancing and retreating blades experience increasing negative loading. Interpreted in terms of fixed wing behavior, to be addressed below, the effect of this loading trend is to decrease the effective span and thus increase the induced drag of the "equivalent wing" representing the rotor.

Vortex Wake Model Analysis and Results

The results with dynamic inflow theory are useful and interesting but leave open a number of questions associated with details of the load distribution and convergence of the results as a function of the number of loading functions. Therefore, it was of interest to generate induced torque results using a prescribed vortex wake model. For the present fundamental investigation, a number of idealizations were included in the modeling of the wake. In fact, the use of a prescribed vortex wake rather than a more accurate "force-free" free wake model was intended to simplify interpretation of results and increase compatibility with the dynamic inflow model that implicitly represents a "prescribed geometry" distribution of wake vorticity. In addition, various options in the prescribed vortex wake model were chosen for similar reasons. In particular, shed components of vorticity were not included and arbitrary choices for the extent of trailed vorticity elements, tip vortex rollup, and vortex element core size

were made. Detailed sensitivity studies were not made to assess the influence of these factors and thus the quantitative results must be considered with these factors in mind.

Results for the effective induced torque using the prescribed vortex wake model are shown in Fig. 18 for combinations of the blade root cutout and blade airfoil stall models. Some combinations of advance ratio and airfoil stall model were not able to achieve trim solutions with the prescribed vortex wake model due to numerical solution convergence issues. Adjustments to the numerical solution analysis options were used to improve the convergence but these options were only pursued to a limited extent. Therefore, results are not presented for the linear airfoil stall model nor for the HS mode branch at high advance ratio.
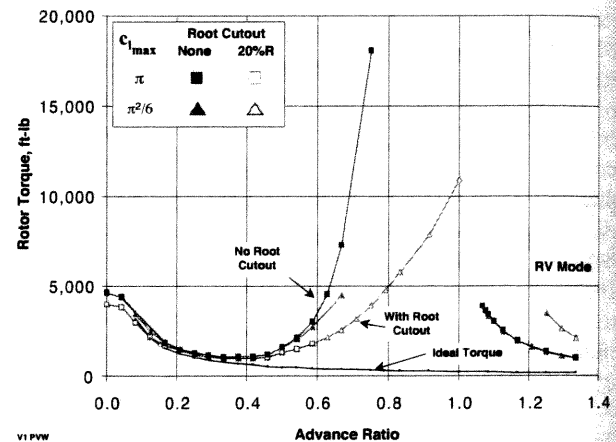

Fig. 18. Rotor effective torque versus advance ratio from prescribed vortex wake inflow model; effect of blade root cutout and stall airfoil models AF2, AF3.

The prescribed vortex wake results in Fig. 18 show trends very similar to the dynamic inflow 9x9 model results. Since the linear airfoil model results are not included, the divergence in induced torque at the critical advance ratio is not in evidence. The result for the blade with root cutout and airfoil stall model AF3 shows the continuous increase of induced torque of the HS mode up to advance ratio 1.0 and operation in the RV mode at high advance ratios for both stall models. The results for advance ratios below 0.2 show unexpected differences for the blades with and without root cutout. The difference persists in hover and in fact both blade configurations show less than the ideal induced hover power calculated for uniform inflow. This is inconsistent for a rotor with untwisted blades, with or without root cutout. The limited vortex wake modeling options that were investigated showed a moderately strong influence at low advance ratios and it is concluded that additional revisions of the vortex wake

modeling parameters are needed to resolve the inconsistent low advance ratio results in Fig. 18.

Comparison of Results from Dynamic Inflow and Prescribed Vortex Wake Models

Rotor Torque Comparisons

A comparison of the effective induced torque results using the dynamic inflow and vortex wake models is presented in Fig. 19. Overall, the results from the two wake models are in relatively close agreement. Both sets of results for the RV mode at high advance are in relatively close agreement. For the blade with root cutout the results are in close agreement at all advance ratios for the HS mode, including the high torque levels at the highest advance ratio. For the blade without root cutout and the AF2 stall model, the torque for the prescribed vortex wake exceeds the dynamic inflow result for moderately high advance ratios. A possible explanation in this case may be related to the influence of root cutout. As will be discussed in the next section, dynamic inflow does not accurately capture the rotor blade airloads and induced velocity near the center of the rotor and the deficiency is more pronounced when the blade root cutout is smallest. In addition, it is possible that the 9x9 dynamic inflow model may not be fully converged at these advance ratios.
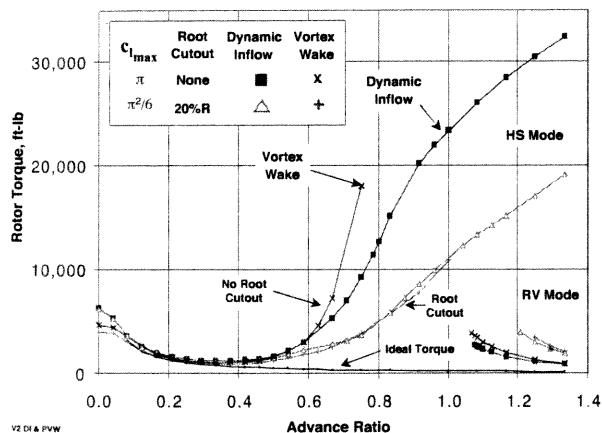

Fig. 19. Comparison of rotor effective torque versus advance ratio from 9x9 dynamic inflow and prescribed vortex wake models; effect of blade root cutout and stall airfoil models AF2, AF3.

At the intermediate advance ratios, where the effects of blade root cutout and airfoil stall model are small, the induced torque of the vortex wake is moderately lower than for dynamic inflow. In hover, dynamic inflow torque exceeds the ideal torque as would be expected. Again these observations reflect the previous comments regarding the vortex wake.

Blade Airload Comparisons

In comparing the rotor induced torque calculated with different induced inflow models, it is useful to include comparisons of the corresponding airload distributions. Representative results for the 0.5 advance ratio condition are presented in Figs. 20 - 23 showing the radial distribution of blade airloads at four azimuths around the rotor disk. The results are for the AF2 airfoil stall model and rotor configurations both with and without blade root cutout. The results are arranged in the form of longitudinal and lateral airload distributions, that is, the longitudinal distributions Figs. 20 and 21 show the 0 and 180 degree azimuth results plotted together on the longitudinal axis of the rotor. Similarly, the lateral airload distributions in Figs. 22 and 23 comprise the 90 and 270 degree azimuths. Several features are evident. First, in comparison to the vortex wake results, the dynamic inflow theory generally captures the principal features of the radial airload distributions except at the ends of the blades in some cases. Second, the vortex wake results show loading variations due to tip vortices not apparent in the dynamic inflow airloads, event though trace evidence of these interactions may be discerned. The principal difference between the two results is that the vortex wake airload distributions "roll-off" more accurately to the zero lift boundary condition at the blade tips and roots. The 9x9 dynamic inflow theory captures this behavior at the blade tips for some azimuths but it is not very successful at the front and retreating blade regions of the rotor disk. In addition there is no evidence of satisfying the zero loading condition at the root of the blade. The most difficult case is the lateral airload distribution without blade root cutout where the blade pitch discontinuity is most pronounced. The vortex wake airloads show the proper trend but do not achieve the zero load boundary condition even though the radial discretization of the blade model is increased at the blade root. The dynamic inflow result shows a discontinuity of considerable magnitude. In the case of the blade root, it is possible that the radial loading functions included in the theory may not be well suited to handle the large blade root airloads that occur in high advance ratio conditions. This is of little consequence at lower advance ratios where the loading at the center of the rotor is very small.

Failure to meet the zero load boundary condition is important for induced drag and torque calculations because a nonzero tip loading implies an infinite induced drag at the tip. Although this does not occur because of numerical discretization of the blade segments, it is nevertheless undesireable as it will likely introduce some degree of error in the numerical results.
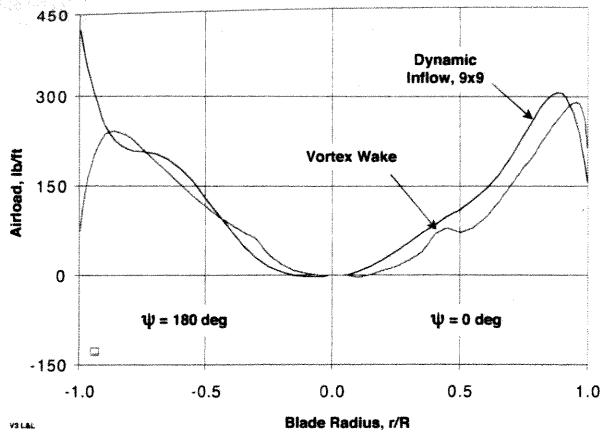
Fig. 20. Comparison of longitudinal distribution of rotor airload from 9x9 dynamic inflow and prescribed vortex wake models without blade root cutout and stall airfoil model AF2, μ=0.5.
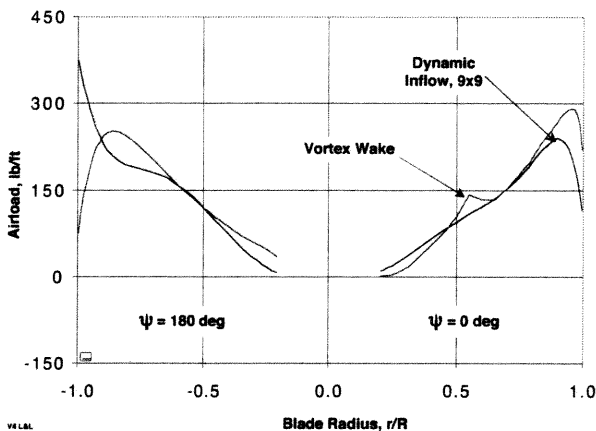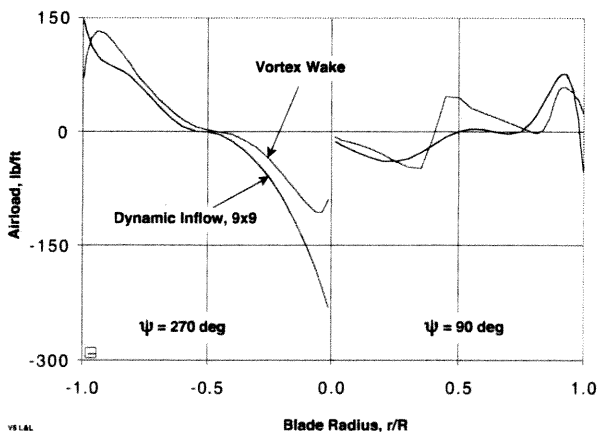

Fig. 21. Comparison of longitudinal distribution of rotor airload from 9x9 dynamic inflow and prescribed vortex wake models with blade root cutout and stall airfoil model AF2, μ=0.5.

Fig. 22. Comparison of lateral distribution of rotor airload from 9x9 dynamic inflow and prescribed vortex wake models without blade root cutout and stall airfoil model AF2, μ=0.5.
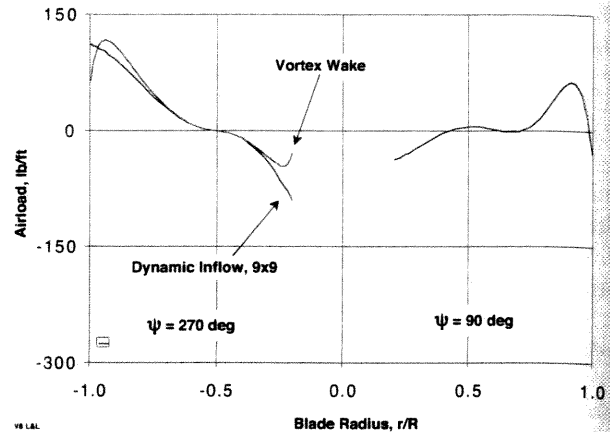

Fig. 23. Comparison of lateral distribution of rotor airload from 9x9 dynamic inflow and prescribed vortex wake models with blade root cutout and stall airfoil model AF2, μ=0.5.

Equivalent Wing Analysis of a Lifting Rotor

This section will explore the relationship between the aerodynamic behavior of the helicopter rotor and the airplane wing, specifically with respect to drag and power due to lift. The underlying justification for the present approach is based on several principles developed by early pioneers in the field of fixed wing aerodynamics that have rarely been applied to the problem of the helicopter rotor. These principles include Munk's stagger theorem and the Trefftz-plane analysis of wing drag-due-to lift. Munk's stagger theorem(s) were originally applied to the problem of optimum (minimum induced drag) loading of biplane wing systems where the upper and lower wings were staggered, one-behind-the-other, in the free-stream direction. One of the original stagger theorems states that the sum of the mutual induced drag components of a biplane wing system having specified spanwise circulation distributions is independent of the amount of wing stagger. The theorem has been extended and generalized by many investigators for a variety of applications. For example, Kroo (Ref. 20) applied a generalized stagger theorem to the analysis of the mutually interfering flowfields of a wing immersed in the wake of a propeller slipstream. As stated: "the net force in the streamwise direction is independent of the streamwise position of surfaces with a given circulation distribution."

The Trefftz-plane analysis is typically applied in steady flow to determine the induced drag of a wing, or system of lifting surfaces arbitrarily distributed in the streamwise, lateral, and vertical directions. The theoretical foundation was developed in the early 1920's (Trefftz, Ref. 21) and it is commonly used today for

finding the induced drag following computation of aerodynamic loading of a lifting surface with potential flow panel methods or a CFD code. The Trefftz-plane is a plane normal to the free-stream direction and far downstream of the lifting system that is cut by the sheet of wake vorticity trailed behind the lifting system. It was first shown by Trefftz that the direct determination of wing induced drag by spanwise integration of the local induced drag distribution was equivalent to the kinetic energy of the free vortex system far downstream of the wing (Ref. 22). In practice, the induced drag based on the energy of the induced flowfield far downstream of the lifting surface is determined by a contour integral along the intersection of the trailing vortex wake with the Trefftz-plane. (Ref. 23). Computationally, this method can more accurate than numerical integration of surface pressure distributions on lifting surfaces.

Based on these basic principles, the following conceptual approach was formulated for determining the induced torque of a lifting rotor. First, it is postulated that there exists a wing with a spanwise distribution of lift equivalent to the lateral distribution of airload acting on the rotor. This wing is called the "equivalent wing." Whereas all points of the wing spanwise lift distribution share the same streamwise location, the airloads acting on the rotating blades of the rotor are distributed across the rotor disk in the streamwise direction. However, based on Munk's stagger theorem, the induced drag of the rotor blade lifting elements is independent of the streamwise location of these elements. This implies that the induced drag of the equivalent wing will be equal to the induced drag of the rotor. An alternative way of expressing this is to say that, far downstream, at the Trefftz-plane, the trailing wake vorticity of the rotor and the equivalent wing will be the same and that, therefore, the induced drag will be the same for each.

To implement this approach, the induced drag of the equivalent wing is determined directly from spanwise lift distribution obtained from the rotor blade radial airload distribution. If the spanwise load distribution is known, it is relatively straightforward to determine the corresponding induced drag using classical Prandtl lifting line theory.

It should be noted that there are several factors that may not be fully accounted for here. These include the effects of periodic unsteady flow in the far wake, the vertical distribution of vorticity in the rotor wake due to oblique flow through the rotor disk at low advance ratio and not included in the planar lifting line theory, and possibly the effects of swirl in the rotor wake.

Equivalent Wing Span Loading

The first step of the present approach is to use the periodic radial distribution of rotor blade airload to determine the periodic spanwise lift distribution of the equivalent wing.

Consider a rotor with b identical blades rotating at constant angular velocity, omega, with each of the blades carrying a periodic radial distribution of normal force airload, (lb/ft) denoted by $n(r, \psi)$, $0 < r < R$, $\psi = \Omega t$. An equivalent fixed wing will be defined, located at the center of the rotor disk, with the positive spanwise axis, y, coinciding with a rotor blade radial axis, r, when $\psi = \pi/2$. The wing extends from $-R < y < R$ with span $2R$ and carries a spanwise distribution of lift (lb/ft) denoted by $l(y, \psi)$. The transformation of the rotor blade airload to the equivalent wing spanwise lift distribution essentially amounts to projecting the rotor airload on the wing spanwise axis as the blade rotates around the azimuth, ψ. Therefore, for a blade at any azimuth, ψ, the corresponding wing lift may be related to the blade airload as follows:

$$l(y,\psi) = n(r,\psi)/\sin\psi \quad |y| \le R\sin\psi$$
$$l(y,\psi) = 0 \quad |y| > R\sin\psi \tag{6}$$

where $r = y/\sin(\psi)$

As the blade rotates around the azimuth, the blade airload will contribute to wing lift on the positive y axis for $0 < \psi < \pi$ and on the negative y axis for $\pi < \psi < 2\pi$. Note that the wing lift at y will be zero until the blade azimuth increases to the point where $R\sin(\psi) = y$. When $\psi = \pi/2$ and $3\pi/2$, the rotor blade axis coincides with the wing spanwise y axis and the wing spanwise lift distribution is identical to the blade radial airload distribution: $l(y) = n(r)$ and $l(-y) = n(r)$, respectively.

Since the rotor blade airload distribution is periodic, the wing lift distribution will also be periodic. In fact, the harmonic content of the wing spanwise lift distribution may be determined by Fourier analysis; for a b-bladed rotor only the nb harmonic components will exist. For present purposes only the mean value of the equivalent wing spanwise lift distribution is needed and this may be expressed by averaging the wing lift over one period as follows:

$$l(y) = \frac{1}{2\pi} \int_{0}^{2\pi} \frac{n(r,\psi)}{\sin\psi} d\psi \tag{7}$$

For present study, this integration was carried out numerically as a post processing procedure following calculation of the rotor blade periodic airloads. In view of the singular nature of the integrand at $\psi = 0$ and π, the numerical algorithm deserves special attention in order to avoid introducing numerical errors in subsequent steps in the equivalent wing analysis.

This process yields familiar results for simple radial airload distributions. For example, if the blade radial airload is invariant around the azimuth and proportional to radius, the rotor disk loading is equivalent to a uniform pressure loading. The spanwise load distribution of for this loading is simply an elliptical distribution obtained by directly integrating the pressure on the rotor disk at each spanwise location. As will be discussed below, this is the ideal wing spanwise load distribution corresponding to minimum induced drag.

Lifting Line Theory Induced Drag

Prandtl's classical lifting line theory is based on the Kutta-Joukowski theorem ($l = \rho V \gamma$) and Helmholtz vortex theorems. The following outline condenses material found in many aerodynamic textbooks. Representing a wing as a lifting line with a spanwise distribution of bound circulation gives rise to a system of trailed vorticity of strength equal to the spanwise gradient of bound circulation. The Biot-Savart Law is used to calculate the induced downwash from the trailed vorticity. The induced drag at any spanwise location is proportional to the product of the bound circulation and the downwash at that span location. If the spanwise lift distribution is expressed as a Fourier series in terms of theta, where $y/R = cos\,\theta$ ($-R < y < R$ for $\pi > \theta > 0$)

$$l(\theta) = \sum_{n=1}^{\infty} A_n \sin n\theta \qquad (9)$$

Lifting line theory then yields the result that the lift of the wing is determined by the first term of the series:

$$L = \frac{\pi b}{4} A_1 \qquad (10)$$

The first term in the series corresponds to an elliptical distribution of lift in the spanwise coordinate, y.

The induced drag of the wing is given by the following summation:

$$D = \frac{2L^2}{\pi \rho V^2 b^2} \sum_{n=1}^{N} n \left(\frac{A_n}{A_1} \right)^2 \qquad (11)$$

This equation directly relates the induced drag of a wing to the span load distribution. It demonstrates the well known lifting line theory result that the minimum induced drag of a wing occurs when the span loading is elliptical, that is, when only the first harmonic of the lift distribution is present. Departures from the ideal elliptical distribution produce additional non-zero harmonic coefficients that increase induced drag. Thus, the fundamental qualitative characteristic of lifting line theory is that the increment of induced drag greater than the ideal minimum value is related to the degree of non-uniformity of the spanwise lift distribution.

Equivalent Wing Span Loading Results

The equivalent wing approach outlined above is implemented by obtaining the spanwise load distribution of the wing from the rotor blade airloads. A Fourier analysis of the spanwise lift distribution is then performed to determine the lift distribution harmonic coefficients that are used in Eq. (11) to determine the equivalent wing induced drag.

The results of the equivalent wing analysis will be presented in two parts, first the spanwise airloads obtained from the rotor blade radial airload distributions. Then the equivalent rotor induced torque determined from the Prandtl lifting line theory analysis will be presented.
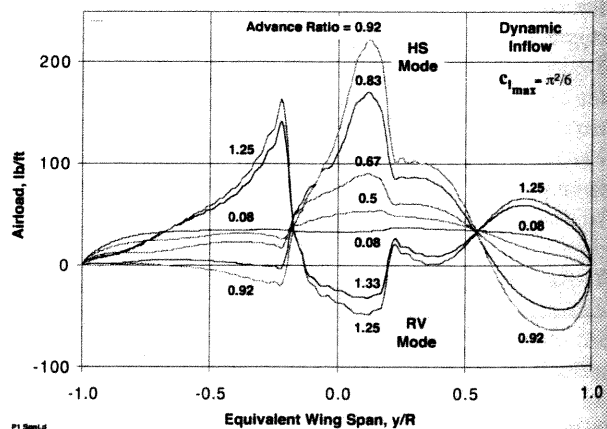

Fig. 24. Equivalent wing spanwise airload distribution based on 9x9 dynamic inflow model, with blade root cutout and AF3 stall airfoil model.

The first results in Fig. 24, based on the rotor airloads from the dynamic inflow 9x9 model, summarize a series of equivalent wing spanwise load distributions corresponding to rotor advance ratios from 0.08 to 1.33 for the configuration with blade root cutout and the AF3 airfoil. Results are included for both the HS and RV modes at high advance ratio. In interpreting these

46

airload distributions it should be noted that magnitude of the load at the center of the "wing" represents not only the rotor airloads near the blade root, but also the blade tip airloads for the rotor azimuths near 0 and 180 degrees. These span load distributions clearly reveal the details of the nonuniform airload as a function of span and advance ratio.

Several of the principal features in Fig. 24 are identified as follows. At low flight speeds, up to about 0.3 advance ratio, the spanwise load distributions are similar to the ideal elliptical loading. At higher speeds the load distribution begins to depart significantly from the elliptical loading and exhibits several distinct nonuniformities. In the case of the HS mode, as advance ratio increases, the airload decreases at the "retreating blade" wing tip while increasing negatively inboard. On the "advancing blade" wing tip, the loading decreases rapidly and then reverses to high negative loads, while the inboard lift increases rapidly with advance ratio. Relatively abrupt loading changes reflect the rotor blade loading discontinuity, associated with blade root cutout for the dynamic inflow model, discussed earlier for Figs. 20 and 23. The predominant feature of the span loading distribution at high advance ratio is the large positive lift in the center of the wing. This reflects the shift in rotor loading away from the advancing and retreating blade tips toward the fore and aft regions of the rotor disk.

It is clear from these span load distributions that, for the HS mode at high advance ratio, the load is carried near the center of the equivalent wing but is shifted toward the "advancing blade" wing tip. This lateral shift acts to counter the high roll moment of the large negative load at the advancing blade wing tip. Figure 24 also includes the span loading for the RV mode at high advance ratio. Interestingly, this distribution is roughly the mirror image of the HS mode distribution. The wing tips carry positive load while the center of the wing is negatively loaded.

Equivalent wing span loading results based on the prescribed vortex wake rotor airloads are presented in Fig. 25. The same rotor blade model is used with blade root cutout and the AF3 airfoil stall model. Overall, the results are very similar to the dynamic inflow calculations in Fig. 24 reflecting that the two analytical approaches largely capture the same basic aerodynamic behavior. The principal difference is in the way the two theories reflect the zero loading boundary conditions at the blade root as discussed earlier. The vortex wake load distributions are considerably smoother for the "advancing blade" side of the wing although not so different for the "retreating blade" side of the wing.
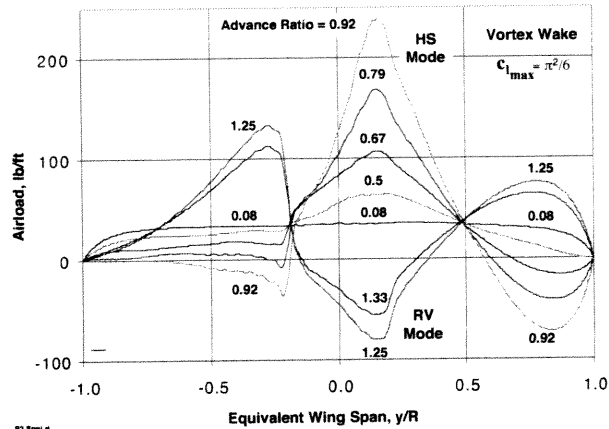

Fig 25. Equivalent wing spanwise airload distribution based on vortex wake inflow model, with blade root cutout and AF3 stall airfoil model.

From the point of view of wing induced drag, the span load distributions in Figs. 24 and 25 imply moderate amounts of non-ideal induced drag at low advance ratios since the loading is roughly elliptical but high induced drag at high advance ratio due to the strong loading nonuniformities. The HS mode loading should produce very high induced drag due to the negative loading at the wing tips, since this will act to drastically reduce the effective span of the wing.

The effect of airfoil stall and blade root cutout might be expected to have a significant impact on the spanwise airload distribution of the equivalent wing. Figure 26 first shows the effect of blade airfoil stall model (AF2 vs AF3) for the wing load distribution of the rotor at high advance ratio. Overall, the effect is relatively small - the airfoil having the higher value of maximum lift coefficient (AF2) produces the larger difference between the peaks of the opposing positive and negative airloads.
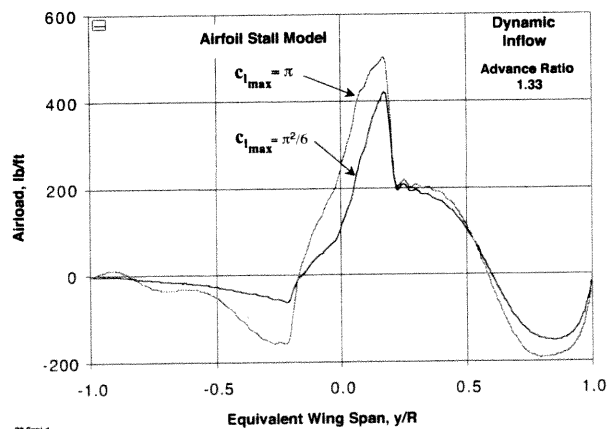

Fig. 26. Effect of stall airfoil model on equivalent wing spanwise airload distribution, 9x9 dynamic inflow model, blade root cutout.

For the dynamic inflow models results, the effects of the blade root cutout are shown in Figs. 27 - 29 for three different operating conditions using the AF2 airfoil. In all three cases, blade root cutout has a pronounced effect. The results show what would appear to be an unrealistic discontinuity in the absence of blade root cutout. With blade root cutout included, the loading discontinuity at the center of the rotor is eliminated, however, large gradients occur for the dynamic inflow model at the edge of the blade root cutout region.

The abrupt discontinuity in the span load distribution at the center of the wing without root cutout is caused by two effects, first the discontinuity in angle of attack of opposing blades at the center of the rotor and, second, the inability of the aerodynamic modeling to properly "smooth" the discontinuity in the resulting airload. The modeling deficiency is relatively pronounced for dynamic inflow theory. The presence of the opposing blade pitch discontinuity may be easily understood for two rotor blades without root cutout for the $\psi = 90$ and 270 deg azimuths. Ignoring the induced inflow, the difference in angle of attack of two blades will be equal to twice the rotor collective pitch (the angle of attack of the retreating blade, trailing edge into the flow, will be the negative of the pitch angle). Since an airload discontinuity cannot physically occur in reality, a valid aerodynamic analysis must generate induced velocity to cancel the blade pitch angle/angle of attack discontinuity without an excessive gradient in the airloading.

Figures 27-29 exhibit oscillatory variations in the span load distribution that are more prominent for the cases without root cutout. These oscillations are numerical artifacts of the algorithm used to transform the rotor airloads to the equivalent wing span loading and the Fourier analysis of the loading.
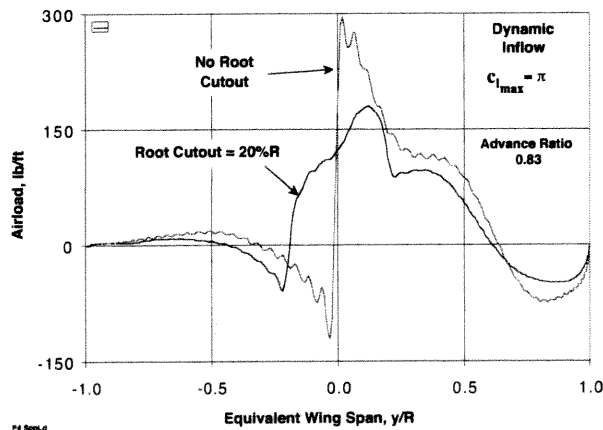

Fig. 27. Effect of blade root cutout on equivalent wing spanwise airload distribution, 9x9 dynamic inflow model and AF2 stall airfoil model, $\mu = 0.83$.
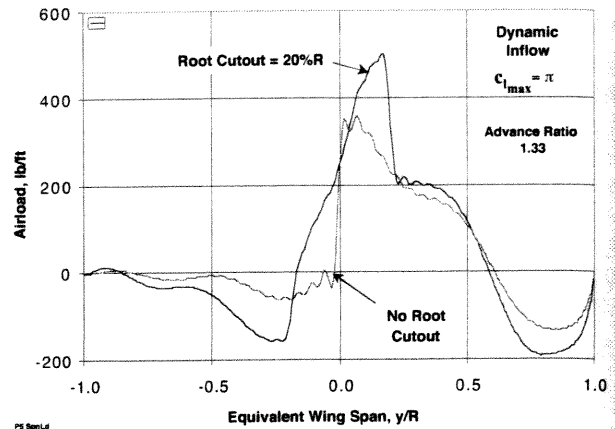

Fig. 28. Effect of blade root cutout on equivalent wing spanwise airload distribution, 9x9 dynamic inflow model and AF2 stall airfoil model, $\mu = 1.33$.
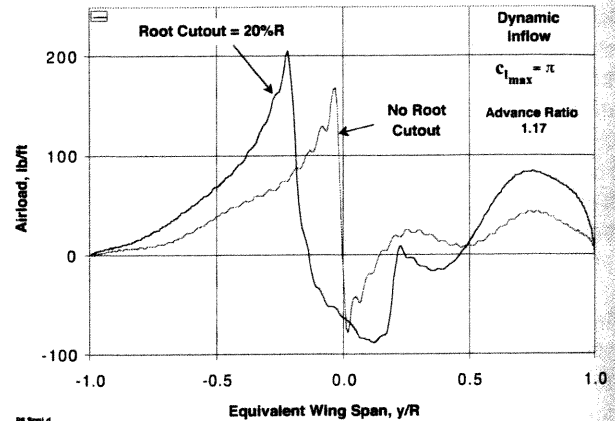

Fig. 29. Effect of blade root cutout on equivalent wing spanwise airload distribution, 9x9 dynamic inflow model and AF2 stall airfoil model, $\mu = 1.17$.

The significance of the effect of blade root cutout on the spanwise load distribution is the potential influence it may have on the induced torque of the rotor. The are several interdependent effects at work here that must be considered. First, the effect of blade root cutout reduces the discontinuity or strong gradient of the spanwise load at the center of the wing. Second, inability of the inflow model (particularly dynamic inflow) to generate a realistic airload distribution across opposing blades at the center of the rotor may contribute to an error in the induced torque. Finally, the results in Figs. 27-29 indicate that, depending on the operating condition, blade root cutout will alter the overall spanwise load distribution in such a way as to increase the spanwise nonuniformity despite the discontinuity at the center of the wing, Fig.29.
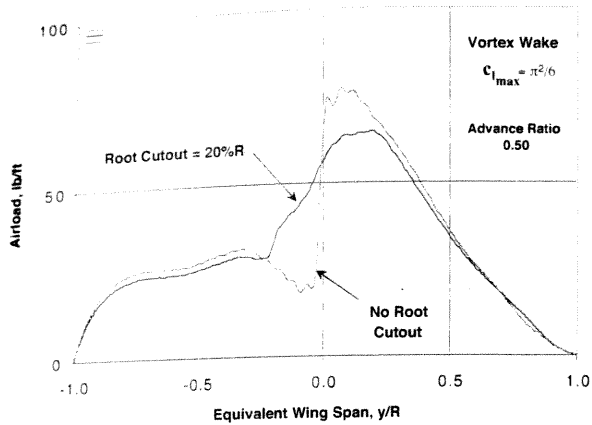
Fig. 30. Effect of blade root cutout on equivalent wing spanwise airload distribution, vortex wake model and AF3 stall airfoil model, $\mu = 0.50$.
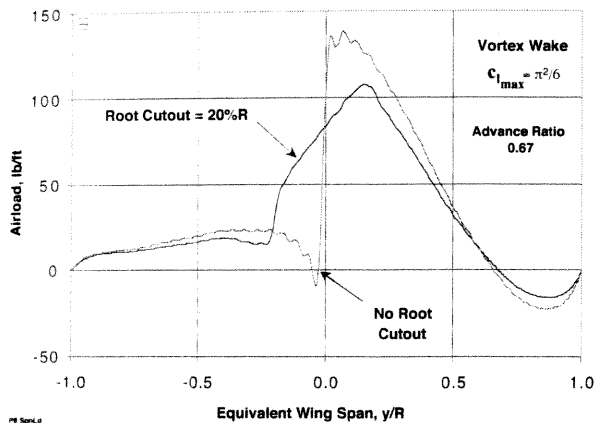

Fig. 31. Effect of blade root cutout on equivalent wing spanwise airload distribution, vortex wake model and AF3 stall airfoil model, $\mu = 0.67$.
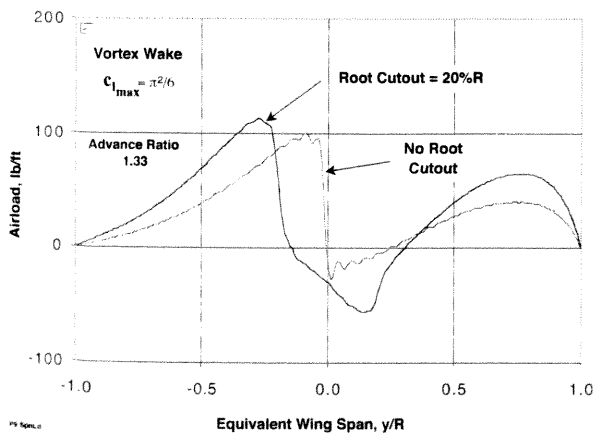

Fig. 32. Effect of blade root cutout on equivalent wing spanwise airload distribution, vortex wake model and AF3 stall airfoil model, $\mu = 1.33$.

The last results compare the effect of blade root cutout on the equivalent wing spanwise loading based on the prescribed vortex wake model, Fig. 30-32. A strong gradient in span loading at the center of the wing remains, but the peak on the "advancing blade" side of the wing is substantially reduced compared to the dynamic inflow results. The peak on the "retreating blade" side of the wing largely remains, however.

Equivalent Wing Induced Torque Results

This section presents the results for the effective induced torque of a rotor based on the calculation of the induced drag of the equivalent wing having a spanwise airload distribution taken from the rotor disk distributed airloads.

Using the equivalent wing induced drag obtained from Eq. (11) above, the effective rotor torque is given by

$$Q_e = DV / \Omega \qquad (12)$$

The results for the dynamic inflow airload calculations for the rotor with blade root cutout and three different airfoil stall models are given in Fig. 33. In accordance with the previous discussion, the blade root cutout configuration is considered to be more appropriate for dynamic inflow model. Furthermore, slow convergence of the series summation of the airload Fourier coefficients in Eq. (11) tends to compromise the numerical accuracy of resulting induced drag calculation for the loading distributions without blade root cutout.
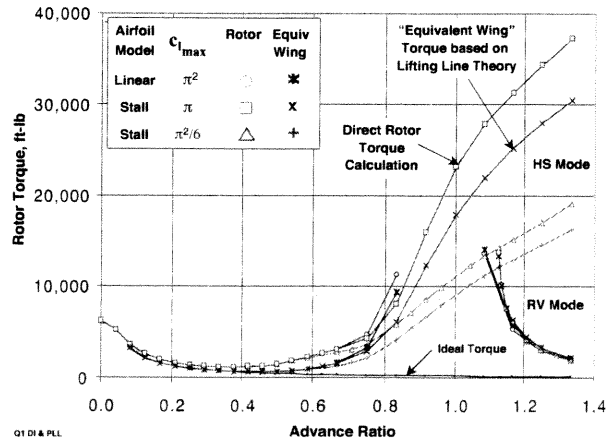

Fig. 33. Comparison of effective torque from rotor and equivalent wing calculations, based on 9x9 dynamic inflow rotor airloads.

The results in Fig. 31 shows that, in general, the equivalent wing lifting line analysis results for induced torque faithfully duplicate the qualitative behavior of

49

the rotor analysis results, and, in some cases, produce good quantitative agreement as well. The very high induced torque trends of the HS mode at high advance ratio are reproduced by the equivalent wing lifting line analysis, generally about 15% to 20% less than the direct rotor calculation at the highest advance ratio. At lower advance ratios from 0.5 to 0.75, the difference is closer to 50%. For the RV mode results at high advance ratio, the equivalent wing results are very close to the direct rotor calculation, ranging down to less than 5%.

Corresponding results comparing the equivalent wing lifting line analysis based on the prescribed vortex wake rotor analysis results are presented in Fig. 34. The two analysis methods generally agree more closely than for the dynamic inflow results. For the case with blade root cutout and the AF3 airfoil stall model, the equivalent wing results are qualitatively similar to dynamic inflow at both low and high advance ratio. The results for the case without blade root cutout are in fairly close agreement but this is somewhat misleading because of the lack of complete convergence of Eq. (11)
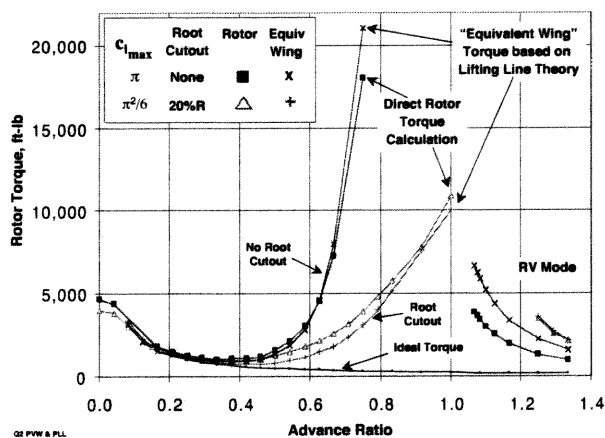

Fig. 34. Comparison of effective torque from rotor and equivalent wing calculations, based on vortex wake inflow rotor airloads.

The present results for the equivalent wing analysis must be considered preliminary given several of the numerical analysis issues noted above. Whether the equivalent wing analysis is valid and practical for quantitative investigation of the induced power characteristics of a rotor remains an open question. Nevertheless, the present results clearly afford a better appreciation for the induced torque characteristics of a rotor, including the influence of diverse operating modes of the rotor on the induced torque. The results in Figs. 33 and 34 may be compared with the equivalent wing span load distributions presented in Figs. 24 to 30 to gain some direct insight into the relationship between

span load distribution and the induced rotor torque. Numerous qualitative associations between the two may be identified.

A few remarks on the relationship between the accuracy of the rotor induced torque calculation and the accuracy of the equivalent wing lifting line analysis may be in order. Since lifting line theory is relatively accurate for simple finite wing aerodynamics, the induced drag (effective torque) of the equivalent wing spanwise airload distribution will be relatively accurate. Whether this result agrees with the rotor analysis will depend on two factors. First, if the basis for the rotor analysis is inaccurate, as would be the case of uniform inflow, for example, both the rotor torque and the rotor airload distribution will be incorrect. And the equivalent wing induced torque, based on the airload distribution, will consequently be incorrect. Moreover, there is no reason to expect the incorrect rotor and equivalent wing results would be the same. Only when the rotor torque and the corresponding airload distribution are both accurate, can the equivalent wing effective induced torque be expected to agree with the direct rotor torque calculation.

Before concluding this section, a final comment on the basic behavior of the induced torque will be offered. One of the initial motivations for the present investigation was to explore and establish the level of non-ideal rotor induced torque. Since the present results are preliminary and relatively limited, few general conclusions may be drawn. However, it seems clear that, for a rotor configuration having untwisted blades with and without blade root cutout, significant levels of non-ideal induced torque occur for relatively moderate advance ratios. For example, at an advance ratio of 0.5, present results indicate that the non-ideal torque is on the order of 1.5 to 2.0 times the ideal induced power. At higher advance ratios these values will increase to factors of 5 to 10 or more for an advance ratio of 0.75 depending on blade root cutout and the airfoil stall model.

Concluding Remarks

In the present investigation, a simplified rotor model and several rotor inflow theories were used to explore fundamental behavior of lifting rotor induced power at moderate and high advance ratios. A number of unusual results were encountered including unusual trim characteristics and very high induced torque at high advance ratios. Not all of the results are fully understood and further interpretation is desired. The results are sensitive to the airfoil model stall characteristics and it is noted that idealized airfoils were

used for the present purposes. Therefore, it is likely that the results are not completely representative of actual airfoil behavior and some of the following conclusions may change depending on the alternative airfoil characteristics. In addition, some of the small anomalies associated with the dynamic inflow and vortex wake results should be resolved. It would also be worthwhile to more fully explore the rotor trim and power results presented herein, including additional parametric results to survey the effects of rotor design parameters on induced power at high advance ratios.

Keeping these caveats in mind, and based on the results presented herein, the following conclusions are drawn:

1. At advance ratio near 1.0, a rotor with linear airfoil characteristics, trimmed with specified lift and zero hub moments, exhibits a reversal in the variation with advance ratio of collective and longitudinal cyclic pitch, associated with the reverse flow region, at a point termed the critical advance ratio.

2. Beyond the critical advance ratio, and with reversed controls, i.e., negative collective pitch, the rotor operates in a mode termed the reverse flow (RV) mode, carrying positive lift in the reverse flow region.

3. For two nonlinear airfoils modeling notional stall behavior, the trim controls increase with advance ratio without a discontinuous reversal. At high advance ratio, the rotor carries negative lift in the reverse flow region and on the advancing blade that is offset by positive lift at the front and rear of the rotor disk. This is termed the high speed (HS) mode.

4. With the nonlinear airfoils, the rotor exhibits multiple trim solutions, also exhibiting trimmed operation in the RV mode with reversed controls.

5. With the nonuniform inflow models, the rotor non-ideal induced torque increased significantly at moderately high advance ratios near 0.5 and above, to the point that the total induced torque increased with advance ratio, unlike the inverse variation with advance ratio of ideal induced torque.

6. For advance ratios approaching the critical advance ratio, the induced torque increased to very high levels, thereafter subsiding above the critical advance ratio in the case of the linear airfoil model operating in the RV mode. Neither the existence, nor the peak value of the induced torque at the critical advance ratio was established.

7. For the nonlinear airfoil models with notional stall behavior, the high induced torque continued to increase beyond advance ratio 1.0 in the HS mode. The alternate trim solution in the RV mode showed much lower torque levels similar to the results based on the linear airfoil model.

8. The high rotor torque levels at high advance ratio are associated with concentration of the airload distribution to the front and rear of the disk. This concentration of loading progresses along with the induced torque at advance ratios beyond 1.0. In the RV mode, at the same advance ratio, the airload is carried on the advancing and retreating sides of the rotor disk and the induced torque is much lower.

9. The induced power results calculated with the dynamic inflow and prescribed vortex wake models were generally in agreement. Some differences were associated with the characteristics of the dynamic inflow theory.

10. An exploration of the application of Prandtl's fixed wing lifting line theory to the determination and interpretation of rotor induced torque characteristics. In general the approach was successful in that the large variations in induced torque at high advance ratio obtained from the rotor analysis were well captured by the equivalent wing analysis. The results were in close agreement for the RV mode.

11. At low and moderate advance ratios, the induced torque trends of the rotor and equivalent wing were qualitatively similar but not as satisfactory quantitatively.

12. The equivalent wing analysis provided considerable insight about the spanwise distribution of airload on a lifting rotor. The relationship between induced torque and the nonuniformities of the span load distribution was clearly evident. The reason for the widely different levels of induced torque in the HS and RV modes was easily observed in terms of the concentration of loading at the center of the rotor or the lateral tips of the rotor and the presence and location of negative loading. The results may be interpreted in terms of an effective span of the rotor.

13. Blade root cutout had a significant effect on trim and induced power characteristics of the lifting rotor at high advance ratio. Blade root cutout increased the value of the critical advance ratio. Blade root cutout reduced the induced power below the critical advance ratio and vice versa.

References

1. Harris, Franklin D., "Rotary Wing Aerodynamics — Historical Perspectives and Important Issues," paper presented at the American Helicopter Society Southwest Region National Specialists Meeting on Aerodynamics and Aeroacoustics, February 25-27, 1987.

2. He, Chengjian, Nelson, Adria, and DuVal, Ronald, "A High Fidelity Rotor Performance Model for Rotorcraft Conceptual Design," paper presented at the 4th Australian Pacific Vertiflite Conference on Helicopter Technology, Melbourne, Australia, July 21-23, 2003.

3. Moffitt, R.C. and Bissell, J.R., "Theory and Application of Optimum Airloads to Rotors in Hoover and Forward Flight," Proceedings of the 38th Annual Forum of the American Helicopter Society, Washington, DC, 1982, pp. 1-12.

4. Quackenbush, T.R., Wachspress, D.A., and Kaufman, A.E., "Optimization of Rotor Performance in Hover Using a Free Wake Analysis," Journal of Aircraft, Vol. 28, No. 3, 1991, pp. 200-207.

5. Hall, S. R., Yang, K.Y., and Hall, K.C., "Helicopter Rotor Lift Distributions for Minimum-Induced Power Loss," Journal of Aircraft, Vol. 31, No. 4, 1994, pp.873-845.

6. Rand, O., Khromov, V., and Peyran, R.J., "Minimum-Induced Power Loss of a Helicopter Rotor via Circulation Optimization," Journal of Aircraft, Vol. 41, No. 1, 2004, pp.104-109.

7. Bhagwat, M.J. and Leishman, J.G., "Rotor Aerodynamics During Maneuvering Flight Using Time Accurate Free-Vortex Wake," Proceedings of the 57th Annual Forum of the American Helicopter Society, Washington, D.C., May 2001.

8. Peters, D. A., and He, Chengjian, "Finite State Induced Inflow Models Part II: Three Dimensional Rotor Disk," Journal of Aircraft, Vol. 32, No. 2, March-April, 1995.

9. Saberi, Hossein; Khoshlahjeh, Maryam; Ormiston, Robert A.; and Rutkowski, M.J., "Overview of RCAS and Application to Advanced Rotorcraft Problems," AHS 4th Decennial Specialist's Conference on Aeromechanics, San Francisco, CA, January 21-23, 2004.

10. Lemont, Harold E., "Technologies for Future Vertical Flight Concepts," Proceedings 56th Annual forum of the American Helicopter Society, Virginia Beach, VA, May 2-4, 2000.

11. Carpenter, P.J., and Fridovich, , B., "Effect of a Rapid Blade Pitch Increase on the Thrust and Induced Velocity Response of a Full Scale Helicopter Rotor," NACA TN 3044, November 1953.

12. Crews, S.T., Hohenemser, K.H., and Ormiston, R.A., "An Unsteady Wake Model for a Hingeless Rotor," Journal of Aircraft, Vol. 10, No. 12, December 1973, pp. 758-760.

13. Curtiss, H.C.,Jr., and Shupe, N.K., "A Stability and Control Theory for Hingeless Rotors," Proceedings of the Annual National Forum of the American Helicopter Society, Washington D.C., May 1971.

14. Mangler, K. W., "Fourier Coefficients for Downwash of a Helicopter Rotor," Royal Aircraft Establishment Report No. Aero. 1958, 1948.

15. Kinner, W., "Theory of the Circular Wing," Ingenieur Archiv, Vol. 7, 1937, pp. 47, Translation No. 2345, Ministry of Aircraft Production, U.K.

16. Pitt, D.M. and Peters, D.A., "Theoretical Prediction of Dynamic-Inflow Derivatives," Vertica, Vol.5, 1981, pp. 21-34.

17. Peters, D.A., and Cao, W.M., "Finite State Induced Inflow Models Part I: Two-Dimensional Thin Airfoil," Journal of Aircraft, Vol. 32, No. 2., March-April, 1995, pp. 313-321.

18. Peters, D.A., and He, Chen Jian, "Finite State Induced Flow Models Part II: Three-Dimensional Rotor Disk," Journal of Aircraft, Vol. 32, No. 2., March-April, 1995, pp. 323-333.

19. Peters, D.A., and Makinen, S.M., "A Comparison of Prandtl and Goldstein Optimum Propeller Solutions with Finite-State Dynamic Wake Models," Georgia Institute of Technology and Army Research Office 10th International Workshop on Aeroelasticity of Rotorcraft Systems, Atlanta, GA, November 3-5, 2003.

20. Kroo, Ilan, "Propeller-Wing Integration for Minimum Induced Loss," AIAA Journal of Aircraft, Vol. 23, No. 7, July 1986, pp. 561-565.

21 Trefftz, E. "The Airfoil and Propellor Theory of Prandtl" (German), Z. agnew. Math Mech., Vol. 1, p. 206, 1921.

22. Prandtl, L., and Tietjens, O. G., "Applied Hydro- and Aeromechanics," Dover Publications, Inc., New York, NY, 1934.

23. Smith, Stephen C. and Kroo, Ilan M., "Computation of Induced Drag for Elliptical and Crescent-Shaped Wings," AIAA Journal of Aircraft, Vol. 30, No. 4., July-August 1993. pp. 446-452.